A Na-rich fluorinated sulfate anti-perovskite with dual doping as solid electrolyte for Na metal solid state batteries

Shengsheng Fan [a,b,1], Meng Lei [b,1], Han Wu [b], Jiulin Hu [b], Congling Yin [a], Tongxiang Liang [a,**], Chilin Li [b,c,*]

[a] College of Material Science and Engineering, Jiangxi University of Science and Technology, Ganzhou, Jiangxi, 341000, China
[b] State Key Laboratory of High Performance Ceramics and Superfine Microstructure, Shanghai Institute of Ceramics, Chinese Academy of Sciences, 585 Heshuo Road, Shanghai, 201899, China
[c] Center of Materials Science and Optoelectronics Engineering, University of Chinese Academy of Sciences, Beijing, 100049, China

ARTICLE INFO

ABSTRACT

High-conductivity solid electrolytes are crucial components for the development of Na-based solid state batteries. However the electrolyte structure prototype and corresponding synthesis method are still lacking. The conventional oxide and sulfide electrolytes are precursor-expensive (e.g. Na_2S) or energy-intensive in sintering synthesis (e.g. at 1000 °C). Here, we propose a novel anti-perovskite solid electrolyte of Na-rich fluorinated sulfate (Na_3SO_4F) benefiting from Mg and Cl co-doping by solid state reaction from low-cost precursors at moderate temperature (500 °C). The tailored dual doping enables an improvement of ionic conductivity by three orders of magnitude close to 10^{-4} S cm^{-1} at 60 °C. The creation of Na vacancies (by aliovalent Mg doping) and lattice expansion (by substituting F sites with larger-sized Cl ions) are responsible for the conductivity upgrade. A Na–Sn/Fe [$Fe(CN)_6$]$_3$ solid state battery based on $Na_{2.98}Mg_{0.01}SO_4F_{0.95}Cl_{0.05}$ electrolyte can reversibly run with a first discharge capacity as high as 91.0 mAh g^{-1} and a reversible capacity preserved at 77.0 mAh g^{-1}. This result paves a way to novel anti-perovskite family of fluorinated sulfates as potential alkali metal ion solid electrolytes beyond already reported A_3OX (A = Li or Na, X = heavy halogen or hydrogenide anions) anti-perovskites.

1. Introduction

Rechargeable batteries with nonaqueous liquid electrolytes have been widely used in electric vehicles, portable electronics and smart-grid energy storage. However, most the liquid electrolytes are toxic, corrosive and flammable. In addition, they are prone to react with alkali metal anodes to trigger the formation of dendrites, which likely pierces through separator and causes short circuit of battery [1,2]. The difficult stabilization of anode retards the application of alkali metal batteries based on liquid organic electrolytes. Solid inorganic electrolytes have brought promises as they possess high tap density, wide electrochemical window, stable bulk structure, high modulus, dendrite suppression ability and no leakage problem, and can be mass-produced [3–5]. Solid state sodium metal batteries based on these electrolytes have the extra advantage of abundant resource and low cost compared with Li metal ones [6–8].

However, the popularization of Na solid electrolytes is still hindered by the lacking of structure prototypes and interface compatibility.

In the early days, β′′-Al$_2$O$_3$ (Na$_2$O·(5–7) Al$_2$O$_3$) was widely investigated because of its excellent ionic conductivity and high electronic resistivity under high temperature operation. However, its synthesis temperature needs to exceed 1600 °C, and the NaAlO$_2$ impurity phase is prone to form at grain boundaries. The moisture sensitivity of impurities causes a reduction of ionic conductivity [9,10]. Then, NASICON type (e.g. Na$_{1+3x}$Zr$_2$(P$_{1-x}$SiO$_4$)$_3$) electrolytes were paid attention to in view of their conductivities exceeding 10^{-4} S cm^{-1} at room temperature. But their applications have been deeply hindered by the large interface impedance and rapid dendrite penetration across grain boundaries [11, 12]. Recently, sulfide-based conductors, such as cubic Na$_3$PS$_4$, gradually attracted more attentions considering their high ionic conductivity (2 × 10^{-4} S cm^{-1} at room temperature) and low activation energy (27 kJ

mol^{-1}). However, the corresponding capacity of sulfide-based solid state batteries decays very quickly in view of the prevailing of interfacial side reactions and passivation of electrode-electrolyte interfaces [7,13]. Hydride-based Na-ion conductors were also studied during the recent ten years because of the enrichment of structure coordination and symmetry. However, the high-conductivity high-temperature phase cannot be stabilized at low temperature, leading to the degradation of ionic conductivity at room temperature (e.g. $Na_2B_{12}H_{12}$ 1×10^{-7} S cm^{-1} at room temperature) [14,15]. Inspired by lithium-rich anti-perovskites with the formula Li_3OX (X is halogen or mixture of halogens), some sodium-rich counterparts with similar structure have also been discovered, such as Na_3OBr, Na_3OBH_4, to display high ionic conductivity [16–18]. The chemical instability or strong hygroscopicity of halogen or hydride anions would however increase the possibility of undesired structure decomposition or hydration during operation.

In this work, we propose and prepare a novel anti-perovskite phase of Na-rich fluorinated sulfate (Na_3SO_4F) with tailored doping as potential Na-ion solid electrolyte for the first time [19,20]. Although the Na^+ conductivity of Na_3SO_4F of $\sim 10^{-8}$ S cm^{-1} at room temperature is far below the requirement of practical application, its ionic conductivity is improved by three orders of magnitude (reaching to 10^{-5} at 40 °C) when co-doping Mg^{2+} and Cl^-, which are favorable for the creation of more mobile Na vacancies as well as structure expansion respectively. The solid state Na batteries based on this doped Na_3SO_4F electrolyte are successfully operated when coupled with Prussian blue cathode [21]. The modification of sodium anode by forming Na–Sn alloy further improves the discharge capacity (91.0 mAh g^{-1}) and cycling performance (with reversible capacity preserved at 77.0 mAh g^{-1} after 20 cycles).

2. Results and discussion

The Na_3SO_4F sample is prepared by ball-milling and following solid state sintering of stoichiometric amounts of Na_2SO_4 and NaF. The Mg and Cl co-doped sample ($Na_{2.98}Mg_{0.01}SO_4F_{0.95}Cl_{0.05}$, denoted as NMSOFC) is synthesized by adding extra MgF_2 and NaCl precursors. Their X-ray diffraction (XRD) patterns are shown in Fig. 1. The XRD and its Rietveld refinement of undoped sample correspond to the Na_3SO_4F phase of anti-perovskite structure [19,20], as indicated from the small weighted residual factor (wR$_P$, 7.136%) and goodness of fit (GOF, 1.29). The doped sample does not cause the remarkable increase of wR$_P$ and GOF values (10.814% and 1.92 respectively), and a small amount of Na_2SO_4 impurity is contained. The refinement result discloses that the doped Na_3SO_4F has larger cell parameters (a = 18.117 Å, b = 6.9712 Å, c = 11.4772 Å) and volume (1381.1 $Å^3$), compared with pristine Na_3SO_4F (Fig. 1c). Their

corresponding atomic coordinates, occupancy rates and isotropic displacement parameters are listed in Tables S1 and S2. The expansion of cell volume is caused by the doping of Cl^- with larger radius into F^- site.

The cross-section images of scanning electron microscopy (SEM) for doped ceramic pellet are shown in Fig. 2. The sample particles with a size of several microns are tightly connected with each other and even entangled or merged into larger-sized monoliths without evident voids between grains. The ceramic surface is quite smooth only with small and few holes. The solid phase sintering is favorable for the densification of ceramic pellet. To further explore the doping situation of Mg and Cl ions, the element mapping of ceramic cross section by energy dispersive X-ray spectrometer (EDS) is shown in Fig. 2c. All the elements of Na, O, S, F, Cl and Mg in doped Na_3SO_4F are detectable with roughly uniform distribution through the selected cross section. The color degree contrast of mapping is caused by the uneven cross section with the bulging or sinking of some grains. Since the sample was smashed for mapping characterization, the resulting cross section is uneven, showing the shallow coloring in the concave part and deep coloring in the convex part. It causes the appearance of uneven element distribution. In fact, the overall distribution of elements in grains is rather uniform. Note that the doping elements of Cl and Mg have the similar distribution tendency as the skeleton elements, indicating a successful doping of Mg and Cl in Na_3SO_4F. The element fraction from EDS is roughly in accordance with the experimentally designed stoichiometry (Table S3). In order to obtain the more accurate electrolyte composition, we also performed the combined analysis based on inductively coupled plasma optical emission spectrometer (ICP-OES) and ion chromatography (IC). Since one characterization tool cannot detect all the elements in NMSOFC electrolyte, the metal and anion compositions were respectively measured by ICP-OES and IC. As shown in Table S4 based on ICP-OES analysis, the molar ratio of Na: Mg is 3.59:0.01, which is slightly higher than the theoretical ratio (2.98:0.01). From Table S5 based on IC analysis, the ratios of halogen elements and sulfate-ion are very close to the theoretical values. The slightly excess Na and Cl are in accordance with the XRD Rietveld refinement result with the potential formation of minor Na_2SO_4 or NaCl impurities. In summary, the chemical composition of NMSOFC pellet is very close to its stoichiometric ratio.

The impedance spectra of Na_3SO_4F and NMSOFC measured at different temperatures are shown in Fig. 3, and S1. For the former, only one semicircle at high frequencies is observed, followed by evident diffusion tail at low frequencies, indicating a dominant Na-ion conduction behavior. The absence of decoupled second semicircle implies a minor resistance of conduction across grain boundaries. The ionic conductivities of Na_3SO_4F are estimated to be 2.44×10^{-8} S cm^{-1} and 4.54

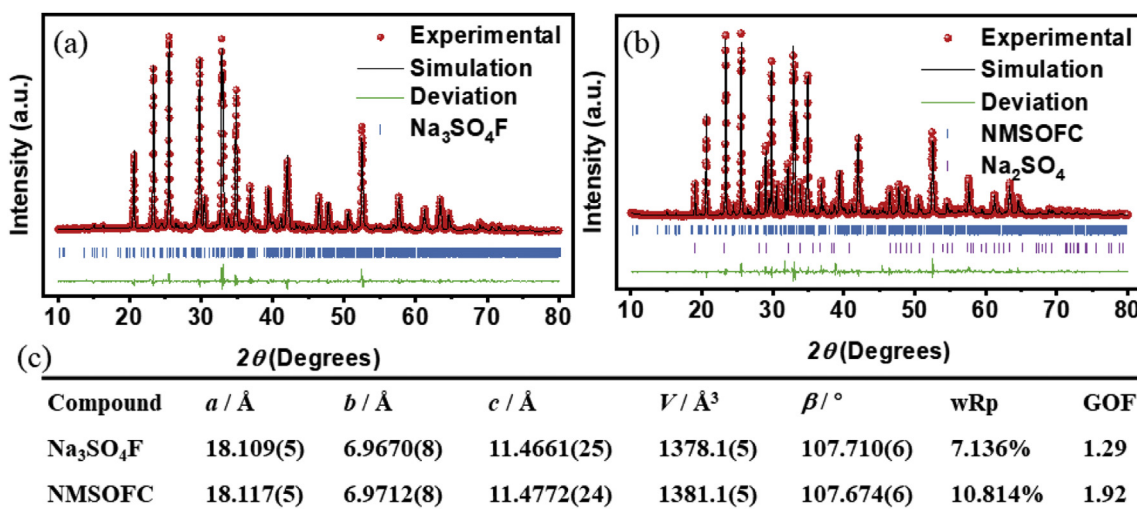| Compound	a / Å	b / Å	c / Å	V / $Å^3$	β / °	wRp	GOF
Na_3SO_4F	18.109(5)	6.9670(8)	11.4661(25)	1378.1(5)	107.710(6)	7.136%	1.29
NMSOFC	18.117(5)	6.9712(8)	11.4772(24)	1381.1(5)	107.674(6)	10.814%	1.92

Fig. 1. XRD patterns and corresponding Rietveld refinement of (a) Na_3SO_4F and (b) NMSOFC. (c) Their crystallographic data and structure refinement parameters.
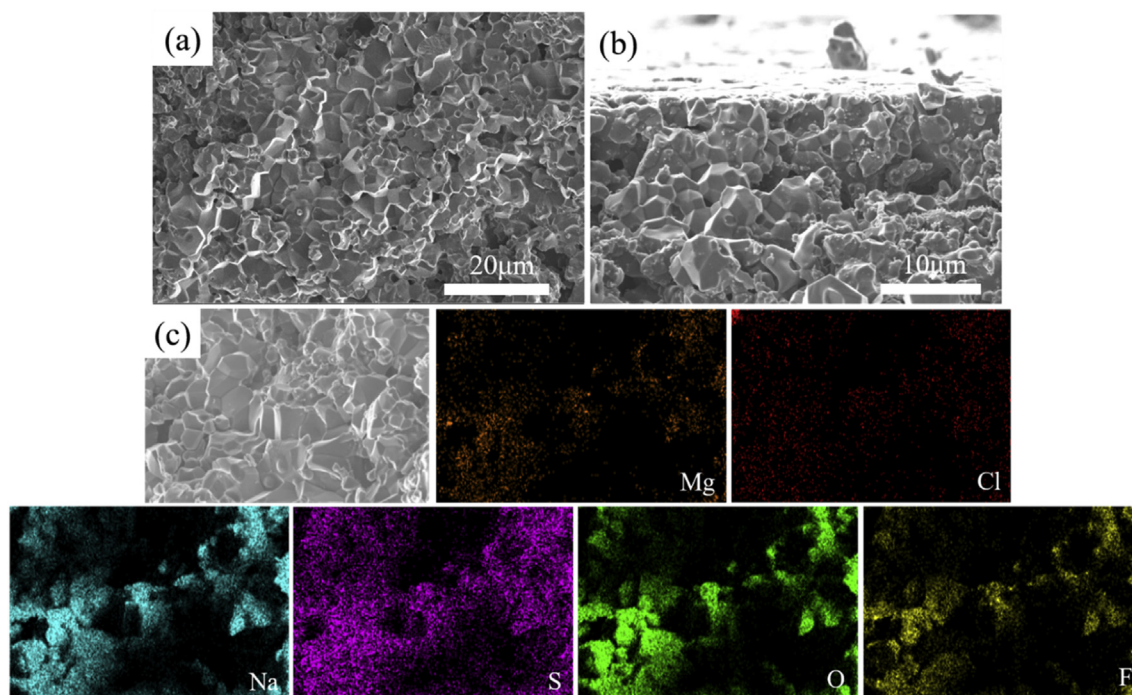
Fig. 2. Cross-section SEM images of NMSOFC pellet focusing on (a) middle and (b) top regions. (c) EDS element mapping of Na, S, O, F, Mg and Cl in NMSOFC.
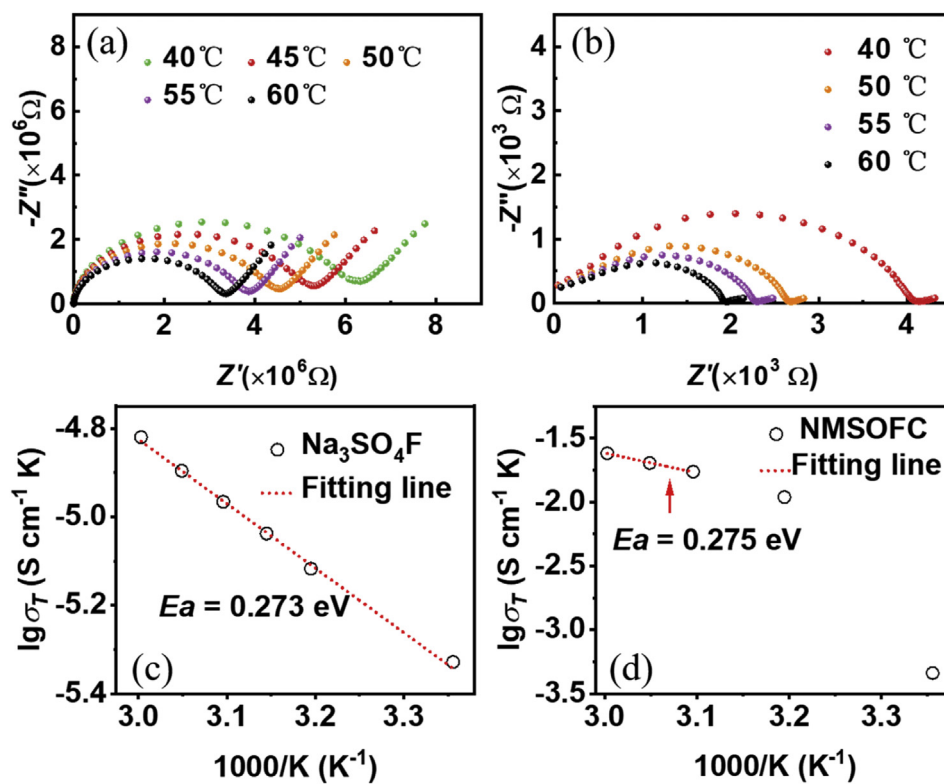

Fig. 3. Nyquist plots of (a) Na$_3$SO$_4$F and (b) NMSOFC solid electrolytes measured at different temperatures. Corresponding Arrhenius plots of (c) Na$_3$SO$_4$F and (d) NMSOFC for estimation of activation energy.

$\times$ 10^{-8} S cm^{-1} at 40 °C and 60 °C respectively. After co-doping, the semicircle becomes slightly depressed mainly at the very high frequencies. This is likely caused by the formation of minor impurities after doping. Benefiting from this dopant combination, the ionic conductivities of NMSOFC at 40 °C and 60 °C are greatly improved to 3.49 $\times$ 10^{-5}

S cm^{-1} and 7.24 $\times$ 10^{-5} S cm^{-1}, respectively. These conductivity values are about three orders of magnitude higher at 40 °C and at 60 °C compared with those of undoped Na$_3$SO$_4$F. Note that the Arrhenius plot at 25 °C for NMSOFC deviates from the linear fitting curve due to the potential defect association in this doped sample, which introduces the

association enthalpy and therefore increases the effective activation enthalpy, leading to the dropping of conductivity value at 25 °C. Doping with divalent cations (Mg^{2+} in this case) requires the formation of sodium vacancies (V'_{Na}) for charge compensation based on the formule: $MgF_2 \rightarrow Mg^{\bullet}_{Na} + V'_{Na} + 2F_F$. At low temperature, defect association would become prominent because of Coulomb interactions between oppositely charged defects based on $Mg^{\bullet}_{Na} + V'_{Na} \rightarrow (Mg^{\bullet}_{Na}, V'_{Na})$, which refers to a bound dopant-vacancy pair [22]. This conductivity deviation phenomenon also indicates a successful heterovalent cation doping in NMSOFC. In contrast, for the undoped sample, all the Arrhenius plots can be linearly fitted in a broader temperature range from 60 to 25 °C. The ionic conductivity values of Na_3SO_4F and NMSOFC at 25 °C are estimated to 1.55×10^{-8} and 1.54×10^{-6} S cm^{-1}, respectively. The latter one is still two orders of magnitude higher compared with the former one, even though it is already discounted by the factor of defect association. The room temperature conductivity of NMSOFC is in the order magnitude of 10^{-6} S cm^{-1}, which is not bad. Since the conductivity at 60 °C is much higher and close to the order magnitude of 10^{-4} S cm^{-1}, therefore we mainly emphasize the cell performance at 60 °C in this manuscript.

As mentioned above, all the Arrhenius plots for Na_3SO_4F are linearly fitted between 60 and 25 °C, with an activation energy (E_a) of 0.273 eV. In view of the influence of defect association in low temperature, the linear fitting of Arrhenius plots for NMSOFC is only effective in a higher temperature region from 60 to 50 °C, leading to an activation energy of 0.275 eV. The comparable E_a values indicate that the doping effect does not remarkably change the migration environment, and the conductivity enhancement is mainly caused by the concentration increase of mobile charge carriers (e.g. Na vacancies). Since the substitution of an aliovalent Mg^{2+} for Na^+ likely results in a positively charged Na vacancy, the enrichment of Na vacancies is expected to increase the ionic conductivity of doped phase. The smaller ion radius and higher polarity of Mg^{2+} is favorable for the trapping and pinning of Mg in the Na sites [23]. On the other hand, some F-ion sites are occupied by larger-sized Cl-ions, which force the lattice expansion of Na_3SO_4F and also accelerate the transport of Na^+. Thermogravimetric and differential thermal analysis (TG-DTA) of NMSOFC at a heating rate of 10 °C min^{-1} in air presents flat curves without weight loss and exothermic peaks as shown in Fig. S2. Different from already reported anti-perovskite electrolytes of halides (e.g. Li_3OCl) and borohydrides (e.g. Na_3OBH_4) [16,18], NMSOFC has good thermal stability up to 500 °C and no phase transition or melting process is observed. This feature endows Na-rich fluorinated sulfate with potentiality as high temperature sodium solid electrolyte.

The kogarkoite Na_3SO_4F can be regarded as a 9R anti-perovskite polytype with a three-dimensional framework, which is constituted by the interconnected $[F_3Na_{12}]$ trimer units through sharing corner (Fig. 4). In each $[F_3Na_{12}]$ trimer, the $[FNa_6]$ octahedra share facets with adjacent

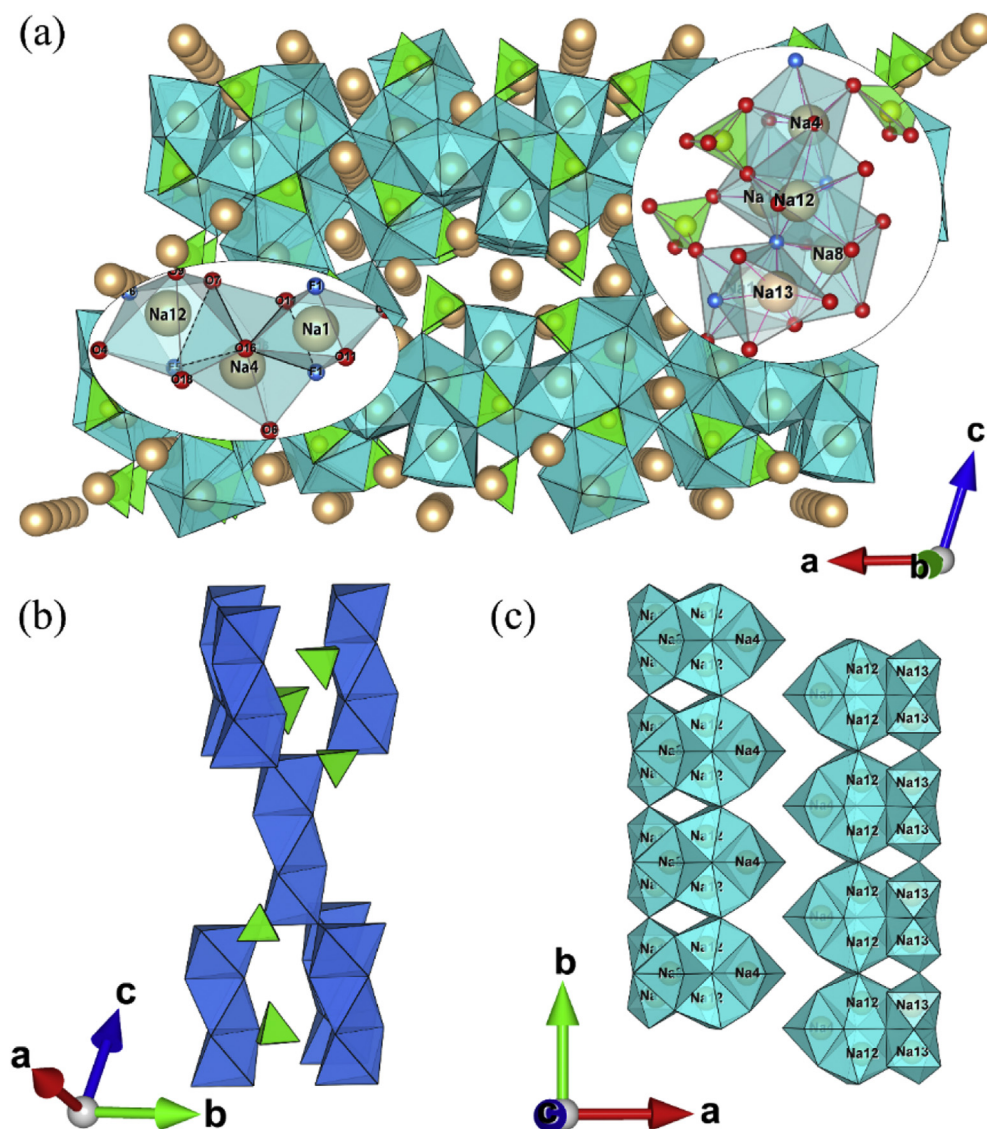**Fig. 4.** (a) Na_3SO_4F structure diagram along b axis, where Na atoms are shown in brown, S in green, F in blue, and O in red. Insets: (left) scenario of two facets of 7-coordinated Na4 are respectively linked to 7-coordinated Na12 and 6-coordinated Na1 in a coplanar manner, (right) scenario of six capped polyhedra are connected by sharing triangle planes to form a polyhedron cluster. (b) A view of interconnected $[F_3Na_{12}]$ trimers by sharing vertex, and $[FNa_6]$ octahedra and $[SO_4]$ tetrahedra are denoted in blue and green colors respectively. In each $[F_3Na_{12}]$ trimer, $[FNa_6]$ octahedra share facets with adjacent octahedra. Discrete $[SO_4]^{2-}$ tetrahedra are located in framework cavities, and are coordinated with 12 Na cations. (c) Illustration of polyhedron clusters along c axis to illuminate how they are linked with each other by sharing-edge along b axis. (For interpretation of the references to color in this figure legend, the reader is referred to the Web version of this article.)

octahedra. The discrete $[SO_4]^{2-}$ tetrahedra are located in the framework cavities, and are coordinated with 12 Na cations. Most of sodium ions coordinated with O or F have a coordination number of 6 or 7, except from Na 2 site, which has an unusual coordination number of 8 (Table S6). Due to the smaller average distance of Na–O(F) bonds, the 6-coordinated Na-ions are more tightly confined to their equivalent sites, compared with 7-coordinated ones. Thus, the ionic conductivity is expected to be dominated by the movement of 7-coordinated Na ions in capped octahedral environment. As shown in the inset of Fig. 4a, two facets of 7-coordinated Na4 are respectively linked to 7-coordinated Na12 and 6-coordinated Na1 in a coplanar manner. The lengths of three sides in the facet shared by Na12 and Na4 based polyhedra are 3.22 (3) Å (for O16–O7), 3.38 (4) Å (for F5–O16), 3.14 (5) Å (for F5–O7) respectively; while the lengths of those shared by Na 4 and Na1 based polyhedra are 2.65 (4) Å (for F1–O11), 2.93 (3) Å (for O11–O16), 3.22 (3) Å (for F1–O16). The triangular facet facing 7-coordinated polyhedra

(e.g. based on central Na12) is larger than that facing 6-coordinated one (e.g. based on central Na1). In the same situation, the triangular facet between Na8 and Na13 centered polyhedra is larger than that between Na8 and Na11 centered polyhedra.

Note that six capped polyhedra are connected by sharing the triangle planes to form a polyhedron cluster (inset of Fig. 4a). In this cluster, the anions (F^- or O^{2-}) in the shared triangle plane are about 3 Å apart in average. In respect of the sizes of oxygen ions of about 1.22 Å and 6-coordinated F-ions of 1.33 Å, a cavity on the triangle center is estimated to be ~0.5 Å in radius. Since the size of cavity in its stable state is smaller than the Na-ion radius (~1 Å) based on 6 or 7 coordination environments, it is deformable when acting as the tunnel of Na^+ transport between these polyhedra. These clusters connect with each other via corners along a and c-axis, which are therefore unfavorable for Na-ion mobility (Fig. S3). The interconnection of polyhedron clusters behaves in a co-edge manner along b axis. The shared edges are 3.65 Å in length
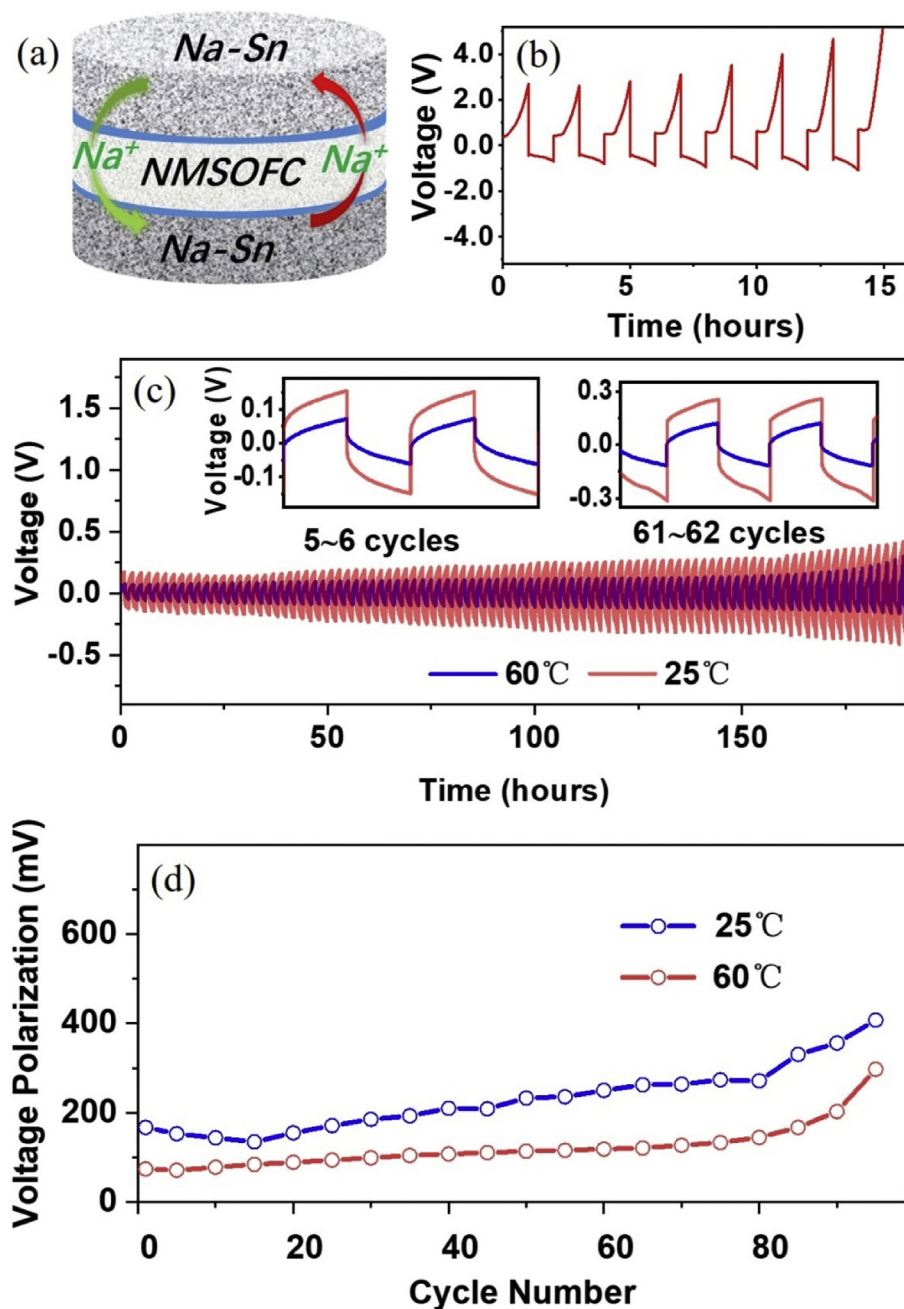

Fig. 5. (a) Schematic of Na–Sn/NMSOFC/Na–Sn symmetric cell with IL wetting at anode-electrolyte interfaces. (b) Plating and stripping voltage profiles of Na/NMSOFC/Na symmetric cell at a current density of 0.05 mA cm^{-2} at 60 °C. (c) Plating and stripping voltage profiles of Na–Sn/NMSOFC/Na–Sn symmetric cell measured at different temperatures of 25 and 60 °C. Insets: Magnified curves of symmetric cell at different cycling stages. (d) Voltage polarization values of Na–Sn/NMSOFC/Na–Sn symmetric cell as a function of cycle number at 25 and 60 °C.

and they shape a cavity of 0.6 Å in radius, which is suitable for Na-ion transport, as shown in Fig. 4c. Therefore a quasi-1D transport mechanism in Na_3SO_4F phase is suggested. The Cl and Mg doping enables the mitigation of spatial hindrance effect in view of potential ligand expansion and Na-vacancy formation.

The availability of fluorinated sulfate anti-perovskite as novel solid electrolyte is indicated by the cycling experiments of Na–Sn/Na–Sn symmetric cells based on Na_3SO_4F and NMSOFC (Figs. 5 and S4). Here the Na-based alloy was adopted as anode by displacing pure Na metal because of the better effect for the former [24,25]. The positive effect of NMSOFC on improving the cycling performance at different temperature (25 and 60 °C) is well confirmed. The Na–Sn/Na_3SO_4F/Na–Sn symmetric cells show much larger voltage polarization than that of Na–Sn/NM-SOFC/Na–Sn ones at the corresponding temperatures. The polarization mitigation for the latter one is beneficial from the significant conductivity enhancement. We also compared the cycling performance of Na–Sn with pure Na as anode. The poor interface stability of pure Na flakes in view of uneven thickness and high activity is responsible for the instable Na plating and stripping behavior in Na/NMSOFC/Na symmetric cell with large voltage overpotential (exceeding 5 V after few cycles), leading to quick capacity fading (Fig. 5b). The fluffy surface of Na–Sn alloy with potential elastic softening and weaker ionic interatomic bonding would increase the contact area at anode-electrolyte interface, and is expected to improve the wettability of Na atoms and reduce their reactivity (Fig. S5) [26]. Therefore the stabilization effect of Na–Sn anode cycling is remarkably modified even at room temperature. The voltage polarization values of Na–Sn/NMSOFC/Na–Sn symmetric cell are decreased to less than 100 mV and 200 mV at 60 °C and 25 °C respectively (Fig. 5c and d). With the increase of cycle number, the low polarization performance is well maintained for 90 cycles, and after 90 cycles the polarization values are still as small as 200 and 350 mV at 60 °C and 25 °C respectively. Note that the polarization degradation with the progressing of Na plating-stripping cycling appears to be unavoidable in view of the accumulation of interface side reactions. It is a common phenomenon for most of the anode-electrolyte interfaces. Actually, the combined use of alloyed Na anode (Na–Sn) and doped electrolyte with much higher conductivity (NMSOFC) has remarkably mitigated the voltage polarization, benefiting from the increase and homogenization of Na-ion flux

across interface as well as the alleviation of interface passivation, compared with the single contribution of heteroatom alloying or doping in anode or electrolyte respectively.

The function of NMSOFC as Na-ion solid electrolyte is checked by integrating it into solid state Na batteries. Here the Prussian blue (PB, $Fe_4[Fe(CN)_6]_3$) is employed as Na-storage cathode material in view of its advantages of open framework and high conductivity [27]. Its intercalation-type reaction mechanism has been well clarified based on the electrochemical process of $Fe_4[Fe(CN)_6]_3 + nNa^+ + ne \leftrightarrow Na_nFe_4[Fe(CN)_6]_3$ [28]. Figs. S6 and S7 verify the successful synthesis of Prussian blue phase and its typical charge and discharge curves in liquid electrolyte based on $NaClO_4$ salt. Fig. 6 shows the configuration and cycling performance of Na/NMSOFC/PB cell at a current density of 0.05 mA cm^{-2} at 60 °C. Drops of ionic liquid (1-ethyl-3-methylimidazolium trifluoromethanesulfonimide [EMIM]TFSI containing 0.01 M $NaClO_4$ salt) are added onto NMSOFC pellet to wet its surface and activate the Na-storage capacity. The first discharge capacity for this solid state cell is 83.3 mAh g^{-1}. However, after only 10 cycles, the capacity is attenuated to 34.5 mAh g^{-1} because of the poor interface stability or wettability of pure Na flakes as discussed above. The use of Na–Sn alloy as anode instead of Na metal enables a higher discharge capacity of 91.0 mAh g^{-1} for the solid state cell of Na–Sn/NMSOFC/PB during the first cycle. After 20 cycles, the discharge capacity is still preserved at 77.0 mAh g^{-1}. The coulombic efficiencies are close to 100%. Its charge and discharge profiles are similar to those in the case of liquid electrolyte. The utilization of NMSOFC electrolyte does not degrade the electrochemical curves of PB cathode, and the well-defined plateaus without evident voltage polarization are achievable. The electrochemical performance of solid state batteries driven by this sodium-rich anti-perovskite electrolyte can be further modified by enhancing its bulk ion conductivity and stabilizing its interface transport in future study. Exploring new synthesis methods (e.g. hot-pressing to improve the electrolyte compactability) as well as modulating the dopant combination and concentration in electrolyte grains are expected to enable the further improvement of conductivity performance for this novel polyanion anti-perovskite family. The ion-wiring and wetting of electrolyte grain boundary and anode-electrolyte interface by conductive secondary phase are expected to improve the grain interconnectivity and interface stability in view of
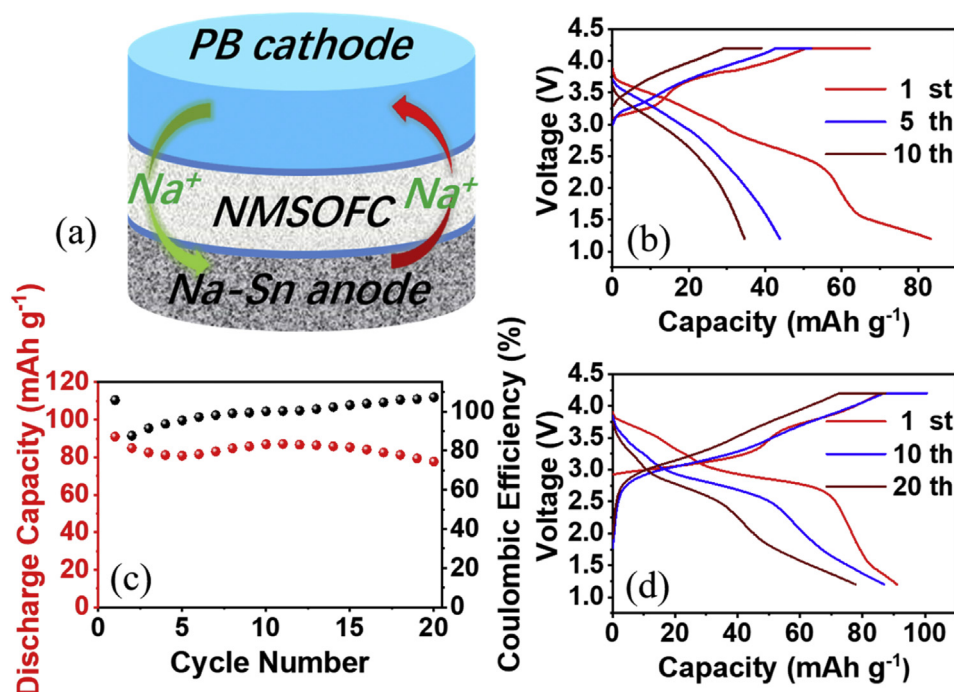

Fig. 6. (a) Schematic of solid-state Na–Sn/NMSOFC/PB cell with IL wetting at electrode-electrolyte interfaces. (b) Charge-discharge curves of Na/NMSOFC/PB cell at various cycling stages at a current density of 0.05 mA cm^{-2} at 60 °C. (c) Specific discharge capacities and coulombic efficiencies as a function of cycle numbers for Na–Sn/NMSOFC/PB cell at a current density of 0.05 mA cm^{-2}. (d) Corresponding charge-discharge curves of Na–Sn/NMSOFC/PB cell at various cycle stages at 0.05 mA cm^{-2}.

the homogenization of Na-ion flux across the interface with Na metal and the suppression of Na anode roughening. The measurement of linear scan voltammetry (LSV) using a Na–Sn/NMSOFC/stainless-steel (SS) asymmetric cell is performed to check the decomposition voltage of this anti-perovskite electrolyte. From Fig. S8, the decomposition voltage is about 4.75 V, indicating a wide electrochemical window for this solid electrolyte. This result is also in accordance with the normal charging phenomenon up to 4.25 V for PB-based full cell. We have to emphasize that the running temperature of 60 °C is not high compared with traditional high-temperature solid state Na batteries with an operation temperature exceeding 150 °C. In the current stage, many solid state batteries have to be operated at enhanced ambience temperature (e.g. 60 °C), e.g. for ones based on popular ceramic and polymer solid electrolytes, since their room temperature performances are not satisfactory. In fact, the feasibility of running at enhanced temperature is an advantage of solid state batteries and can extend their application fields. The liquid electrolyte systems usually cannot sustain high-temperature operation due to their high volatility and flammability as well as the potential acceleration of side reactions.

3. Conclusion

In summary, we have successfully proposed and prepared a novel dual-doped anti-perovskite solid electrolyte of Na-rich fluorinated sulfate (Na_3SO_4F) with ionic conductivities of 7.24×10^{-5} S cm^{-1} and 3.49×10^{-5} S cm^{-1} at 60 °C and 40 °C respectively. The production of more Na vacancies by Mg doping and lattice expansion by Cl doping are responsible for the conductivity increase by three orders of magnitude compared with pristine Na_3SO_4F phase. The Na–Sn/NMSOFC/PB solid cell was successfully operated with a first discharge capacity as high as 91.0 mAh g^{-1} and a reversible capacity preserved at 77.0 mAh g^{-1}. The Na plating/stripping cycling of Na–Sn/NMSOFC/Na–Sn symmetric cell is significantly improved with a polarization overpotential less than 100 mV during the early cycling. Na-rich fluorinated sulfate family with anti-perovskite structure is promising as high-conductivity Na-ion solid electrolyte by further doping and synthesis optimization.

4. Experimental section

4.1. Synthesis of Na₃SO₄F and Na₂.₉₈Mg₀.₀₁SO₄F₀.₉₅Cl₀.₀₅

Na_2SO_4 (Aladdin, 99.9%), NaF (Aladdin, 99.99%) and MgF_2 (Aladdin, 99.99%), NaCl (Shanghai Lingfeng chemical, 99.5%) of stoichiometric amounts were weighted and ball-milled with the aid of alcohol for 12 h at a speed of 300 r min^{-1}. The doping amounts of Mg and Cl ions were set to be 1 mol% and 5 mol% respectively. The mixed slurry was dried overnight at 60 °C, and the dried powder was ground in an agate mortar for 20 min. An appropriate amount of powder was pressed into a pellet with a diameter of 10 mm and a thickness of 1 mm under 10 MPa. The pellets were fired at 500 °C for 36 h in a muffle furnace at a rate of 4 °C min^{-1}, enabling the synthesis of $Na_{2.98}Mg_{0.01}SO_4F_{0.95}Cl_{0.05}$ (MNSOFC). Na_3SO_4F pellets were prepared based on the similar procedures but without the addition of Mg and Cl precursors. The relative densities of NMSOFC and Na_3SO_4F pellets are 88% and 87.7%, respectively.

The phase purity of samples was check by X-ray diffraction technique (XRD). The XRD patterns were collected by Bruker D8 ADVANCE using a Cu Kα source. The Rietveld refinements were carried out using GSAS-Π program packages. Scanning electron microscopy (SEM) images and corresponding component mapping were used to observe the morphology and element distribution of Na_3SO_4F and NMSOFC pellets with FEI Magellan 400 equipped energy dispersive X-ray spectrometry (EDS). The inductively coupled plasma optical emission spectrometer (ICP-OES, Agilent-725) and ion chromatography (IC, ICS-2100) were used to obtain the more accurate electrolyte composition. Thermogravimetric and differential thermal analysis (TG-DTA) was performed by Netzsch STA 409 PC.

4.2. Fabrication of Prussian blue cathodes

In a typical synthesis, 10 mmol $Na_4Fe(CN)_6 \cdot 10H_2O$ (Aladdin, 99.9%) and 5 mL hydrochloric acid (37%) were dissolved in 100 mL deionized water to obtain a homogenous solution. Then the homogenous solution was maintained at 60 °C in water bath for 4 h under vigorous stirring to obtain $Fe_4[Fe(CN)_6]_3$ nanocubes. The compound was collected by filtration, washed by water and ethanol for three times and dried at 100 °C in a vacuum oven for 24 h. The Prussian blue (PB) powder was then mixed with Super P as conductive additive and polyvinylidene difluoride (PVDF, Sigma) as binder in N-methyl-2-pyrrolidone (NMP, Aladdin) solvent in a weight ratio of 7:2:1 to prepare the cathode slurry, After that, the PB cathode was obtained by casting the slurry onto aluminum foil, followed by vacuum drying at 50 °C overnight. Finally the cathode sheet was cut into circular cathode pieces with a diameter of 8 mm.

4.3. Coin cell assembly

The Na/NMSOFC/PB coin cells (CR2032 type) were assembled inside an Ar-filled glove box. Therein ionic liquid (IL, containing 0.01 M NaClO$_4$ in 1-ethyl-3-methylimidazolium trifluoromethanesulfonimide salt [EMIM]TFSI) as wetting agent was dropped onto NMSOFC pellet surface to modify the electrode-electrolyte interfaces. Na–Sn/NMSOFC/PB coin cells were assembled in the same way. Therein Na–Sn alloy as anode was prepared by heating the Na pellet with Sn particles uniformly spread on the surface of Na pellet at 100 °C for 5 min. The Na/PB liquid cell based on 1 M NaClO$_4$ dissolved in ethylene carbonate (EC) and propylene carbonate (PC) with a volume ratio of 1:1 was also assembled as a comparison. The measurement of linear scan voltammetry (LSV) using a Na–Sn/NMSOFC/stainless-steel (SS) asymmetric cell was performed to check the decomposition voltage of the anti-perovskite electrolyte. The symmetric cells of Na/NMSOFC/Na, Na–Sn/NMSOFC/Na–Sn and Na–Sn/Na$_3$SO$_4$F/Na–Sn were also assembled in the configuration of coin cells.

4.4. Electrochemical measurements

The electrochemical cycling test of full cells and symmetric cells were performed on a battery testing system (LAND-CT2001A) at 60 °C. The electrochemical impedance spectra of Na_3SO_4F and NMSOFC solid electrolytes in sandwich structure with Ag electrodes were collected in Solartron frequency analyzer (1260–1296) in a frequency range from 100 kHz to 0.1 Hz with an amplitude of 10 mV. Ionic conductivity values (σ) of Na_3SO_4F and NMSOFC are obtained by the following equation:

$$\sigma = \frac{d}{RS} \quad \quad (1)$$

where d is the thickness of electrolyte pellets, S is the electrode area and R is the electrolyte resistance. The activation energy values are calculated from Arrhenius plots using the equation below:

$$\sigma T = A e^{\left(-\frac{Ea}{kT}\right)} \quad \quad (2)$$

where A, Ea, k, and T correspond to pre-exponential factor, activation energy, Boltzmann constant and absolute temperature, respectively.

Declaration of competing interest

The authors declare no conflict of interest.

CRediT authorship contribution statement

Shengsheng Fan: Investigation, Formal analysis, Writing - original

draft. **Meng Lei:** Investigation, Formal analysis, Writing - original draft. **Han Wu:** Investigation, Formal analysis. **Jiulin Hu:** Investigation, Formal analysis. **Congling Yin:** Supervision, Writing - review & editing. **Tongxiang Liang:** Supervision. **Chilin Li:** Supervision, Conceptualization, Methodology, Writing - original draft, Writing - review & editing.

Acknowledgements

Appendix A. Supplementary data

Supplementary data to this article can be found online at https://doi.org/10.1016/j.ensm.2020.05.030.

References

[1] Q. Yang, C. Li, Li metal batteries and solid state batteries benefiting from halogen-based strategies, Energy Storage Mater 14 (2018) 100–117.
[2] B. Liu, J.-G. Zhang, W. Xu, Advancing lithium metal batteries, Joule 2 (2018) 833–845.
[3] C. Sun, J. Liu, Y. Gong, D.P. Wilkinson, J. Zhang, Recent advances in all-solid-state rechargeable lithium batteries, Nanomater. Energy 33 (2017) 363–386.
[4] Y. Kato, S. Hori, T. Saito, K. Suzuki, M. Hirayama, A. Mitsui, M. Yonemura, H. Iba, R. Kanno, High-power all-solid-state batteries using sulfide superionic conductors, Nat. Energy 1 (2016) 16030.
[5] J.C. Bachman, S. Muy, A. Grimaud, H.H. Chang, N. Pour, S.F. Lux, O. Paschos, F. Maglia, S. Lupart, P. Lamp, L. Giordano, Y. Shao-Horn, Inorganic solid-state electrolytes for lithium batteries mechanisms and properties governing ion conduction, Chem. Rev. 116 (2016) 140–162.
[6] J.-J. Kim, K. Yoon, I. Park, K. Kang, Progress in the development of sodium-ion solid electrolytes, Small Methods 1 (2017) 1700219.
[7] A. Hayashi, K. Noi, A. Sakuda, M. Tatsumisago, Superionic glass-ceramic electrolytes for room-temperature rechargeable sodium batteries, Nat. Commun. 3 (2012) 856.
[8] W. Zhou, Y. Li, S. Xin, J.B. Goodenough, Rechargeable sodium all-solid-state battery, ACS Cent. Sci. 3 (2017) 52–57.
[9] N. Li, Z.Y. Wen, Y. Liu, X.G. Xu, J. Lin, Z.H. Gu, Preparation of Na-beta-alumina film by tape casting process, J. Eur. Ceram. Soc. 29 (2009) 3031–3037.
[10] S.T. Lee, D.H. Lee, S.M. Lee, S.S. Han, S.H. Lee, S.K. Lim, Effects of calcium impurity on phase relationship, ionic conductivity and microstructure of Na+-β/β''-alumina solid electrolyte, Bull. Mater. Sci. 39 (2016) 729–735.
[11] Q. Ma, M. Guin, S. Naqash, C.-L. Tsai, F. Tietz, O. Guillon, Scandium-substituted $Na_3Zr_2(SiO_4)_2(PO_4)$ prepared by a solution-assisted solid-state reaction method as sodium-ion conductors, Chem. Mater. 28 (2016) 4821–4828.
[12] Z. Zhang, Z. Zou, K. Kaup, R. Xiao, S. Shi, M. Avdeev, Y. Hu, D. Wang, B. He, H. Li, X. Huang, L.F. Nazar, L. Chen, Correlated migration invokes higher Na^+-ion conductivity in NaSICON-type solid electrolytes, Adv. Energy Mater. (2019), https://doi.org/10.1002/aenm.201902373.
[13] Z. Zhu, I.-H. Chu, Z. Deng, S.P. Ong, Role of Na^+ interstitials and dopants in enhancing the Na^+ conductivity of the cubic Na_3PS_4 superionic conductor, Chem. Mater. 27 (2015) 8318–8325.
[14] N. Verdal, T.J. Udovic, V. Stavila, W.S. Tang, J.J. Rush, A.V. Skripov, Anion reorientations in the superionic conducting phase of $Na_2B_{12}H_{12}$, J. Phys. Chem. C 118 (2014) 17483–17489.
[15] W.S. Tang, M. Matsuo, H. Wu, V. Stavila, A. Unemoto, S. Orimo, T.J. Udovic, Stabilizing lithium and sodium fast-ion conduction in solid polyhedral-borate salts at device-relevant temperatures, Energy Storge Mater 4 (2016) 79–83.
[16] Y. Zhao, L.L. Daemen, Superionic conductivity in lithium-rich anti-perovskites, J. Am. Chem. Soc. 134 (2012) 15042–15047.
[17] H. Nguyen, S. Hy, E. Wu, Z. Deng, M. Samiee, T. Yersak, J. Luo, S.P. Ong, Y.S. Meng, Experimental and computational evaluation of a sodium-rich anti-perovskite for solid state electrolytes, J. Electrochem. Soc. 163 (2016) A2165–A2171.
[18] Y. Sun, Y. Wang, X. Liang, Y. Xia, L. Peng, H. Jia, H. Li, L. Bai, J. Feng, H. Jiang, J. Xie, Rotational cluster anion enabling superionic conductivity in sodium-rich antiperovskite Na_3OBH_4, J. Am. Chem. Soc. 141 (2019) 640–5644.
[19] M.S. Avdontceva, A.A. Zolotarev, S.V. Krivovichev, Order–disorder phase transition in the antiperovskite-type structure of synthetic kogarkoite, Na_3SO_4F. J. Solid State Chem. 231 (2015) 42–46.
[20] L. Fanfani, G. Giuseppetti, C. Tadini, P.F. Zanazzi, The crystal structure of kogarkoite, Na_3SO_4F. Mineral. Mag. 43 (1980) 753–759.
[21] Y. You, X.-L. Wu, Y.-X. Yin, Y.-G. Guo, High-quality Prussian blue crystals as superior cathode materials for room-temperature sodium-ion batteries, Energy Environ. Sci. 7 (2014) 1643–1647.
[22] P. Knauth, H.L. Tuller, Solid-state ionics: Roots, status, and future prospects, J. Am. Ceram. Soc. 85 (2002) 1654–1680.
[23] J. Tian, D. Cao, X. Zhou, J. Hu, M. Huang, C. Li, High-capacity Mg-organic batteries based on nanostructured rhodizonate salts activated by Mg-Li dual-salt electrolyte, ACS Nano 12 (2018) 3424–3435.
[24] Y. Tian, T. Shi, W.D. Richards, J. Li, J.C. Kim, S.H. Bo, G. Ceder, Compatibility issues between electrodes and electrolytes in solid-state batteries, Energy Environ. Sci. 10 (2017) 1150–1166.
[25] X. Chi, Y. Liang, F. Hao, Y. Zhang, J. Whiteley, H. Dong, P. Hu, S. Lee, Y. Yao, Tailored organic electrode material compatible with sulfide electrolyte for stable all-solid-state sodium batteries, Angew. Chem. Int. Ed. 57 (2018) 2630–2634.
[26] M. Mortazavi, J. Deng, V.B. Shenoy, N.V. Medhekar, Elastic softening of alloy negative electrodes for Na-ion batteries, J. Power Sources 225 (2013) 207–214.
[27] J. Qian, C. Wu, Y. Cao, Z. Ma, Y. Huang, X. Ai, H. Yang, Prussian blue cathode materials for sodium-ion batteries and other Ion Batteries, Adv. Energy Mater. 8 (2018) 1702619.
[28] H. Sun, H. Sun, W. Wang, H. Jiao, S. Jiao, $Fe_4[Fe(CN)_6]_3$: a cathode material for sodium-ion batteries, RSC Adv. 4 (2014) 42991–42995.